

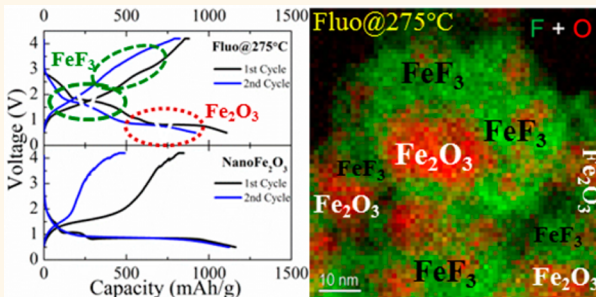
Controlled Formation of Mixed Nanoscale Domains of High Capacity Fe_2O_3 – FeF_3 Conversion Compounds by Direct Fluorination

Hui Zhou,^{*,†} Rose E. Ruther,[†] Jamie Adcock,[‡] Wu Zhou,[†] Sheng Dai,^{*,§} and Jagjit Nanda^{*,†,⊥}

[†]Materials Science and Technology Division, and [§]Chemical Sciences Division, Oak Ridge National Laboratory, Oak Ridge, Tennessee 37831, United States and

[‡]Department of Chemistry, and [⊥]Bredesen Centre for Interdisciplinary Science & Graduate Education and Department of Chemical and Biomolecular Engineering, University of Tennessee, Knoxville, Tennessee 37996, United States

ABSTRACT We report a direct fluorination method under fluorine gas atmosphere using a fluidized bed reactor for converting nanoparticle iron oxide ($n\text{-Fe}_2\text{O}_3$) to an electrochemically stable and higher energy density iron oxyfluoride/fluoride phase. Interestingly, no noticeable bulk iron oxyfluoride phase (FeOF) phase was observed even at fluorination temperature close to 300 °C. Instead, at fluorination temperatures below 250 °C, scanning transmission electron microscopy coupled with electron energy loss spectroscopy (STEM-EELS) and X-ray photoelectron spectroscopy (XPS) analysis showed surface fluorination with nominal composition, $\text{Fe}_2\text{O}_{3-x}\text{F}_{2x}$ ($x < 1$). At fluorination temperatures of 275 °C, STEM-EELS results showed porous interconnected nanodomains of FeF_3 and Fe_2O_3 coexisting within the same particle, and overall the particles become less dense after fluorination. We performed potentiometric intermittent titration and electrochemical impedance spectroscopy studies to understand the lithium diffusion (or apparent diffusion) in both the oxyfluoride and mixed phase $\text{FeF}_3 + \text{Fe}_2\text{O}_3$ composition, and correlate the results to their electrochemical performance. Further, we analyze from a thermodynamical perspective, the observed formation of the majority fluoride phase (77% FeF_3) and the absence of the expected oxyfluoride phase based on the relative formation energies of oxide, fluoride, and oxyfluorides.



KEYWORDS: conversion electrode · fluorination · nano- Fe_2O_3 · fluoride

Multivalent conversion-based binary transition metal (TM) compounds have recently gained significant attention because of their higher specific capacity compared to conventional intercalation-based lithium-ion materials. Multiple redox states available due to transition metal 3d levels contribute toward transfer of greater than one lithium per transition metal atom.¹ Additionally, most of the high capacity transition metal binary conversion compounds are naturally abundant, nontoxic, and have redox potentials that lie within the voltage window of standard electrolytes.^{2–8} However, harvesting high reversible capacity from multivalent systems is difficult because of a number of materials challenges. These include low electronic conductivity, poor diffusion, and

interfacial kinetics, and structural instability during multielectron charge transfer.^{9–17} These difficulties lead to poor cycle life and a large voltage hysteresis which make conversion compounds unsuitable for any practical application at present.

One important class of conversion compounds that has attracted wide attention is the iron oxides (Fe_2O_3 and Fe_3O_4). However, their low redox plateau (<2 V vs Li/Li⁺) typically makes them suitable only as anode materials for lithium battery applications.^{1,18–21} Compared to oxides, fluorides have higher redox voltages, mainly due to the higher ionicity of the metal–fluoride bonds, which makes them promising alternatives for cathode materials.^{14,15,22–25} Unfortunately, the high ionicity of these materials also results in low electronic conductivity,

* Address correspondence to
nanda@ornl.gov;
nyhzhou@gmail.com.

Received for review September 11, 2014
and accepted February 21, 2015.

Published online February 22, 2015
10.1021/acsnano.5b00191

© 2015 American Chemical Society

TABLE 1. Experimental Conditions for the Fluorination Process and Weight Increase after Fluorination^a

	F ₂ flow rate	reaction time	initial weight	% wt gain	% Fe ₂ O ₃ reacted	formula (bulk)	formula (surface)
NanoFe ₂ O ₃						Fe ₂ O ₃	Fe ₂ O _{3.11}
Fluo@175 °C	3.2 sccm	22 h	1.999 g	4.0%	9.6%	Fe ₂ O _{2.71} F _{0.58}	Fe ₂ O _{2.33} F _{1.66}
Fluo@225 °C	3.2 sccm	22 h	1.999 g	8.8%	21.3%	Fe ₂ O _{2.36} F _{1.28}	Fe ₂ O _{1.78} F _{2.72}
Fluo@275 °C	3.2 sccm	24 h	1.902 g	29.1%	70.3%	Fe ₂ O _{0.89} F _{4.22}	Fe ₂ O _{0.43} F _{4.47}

^aThe chemical formulas of the fluorinated samples were calculated from weight gain (average or bulk composition) and XPS data (surface composition only).

which greatly limits their electrochemical performance. To overcome this issue, oxyfluoride phases were proposed by a few groups and showed significant improvement including greater electrochemical capacity retention and reduced voltage hysteresis. The coexistence of M-O and M-F bonds reduces the ionicity of the compounds while maintaining the higher redox potential.^{26,27}

The conventional synthesis of iron oxyfluoride is carried out by either heating iron fluoride (FeF₃) and iron oxide (Fe₂O₃)²⁸ or by a reaction using Fe-based precursors where the stoichiometry of oxygen to fluorine inside the oxyfluoride is controlled by synthesis atmosphere, temperature, and time.²⁶ This study demonstrates a novel method where we aim to obtain the oxyfluoride phase from nanosized Fe₂O₃ particles by using fluorine gas in a fluidized bed reactor configuration. At a fundamental level, this approach involves replacing oxygen atoms in Fe₂O₃ partially with fluorine which is contrary to the earlier approach of replacing fluorine atoms in FeF₃ with oxygen.²⁶

Our initial study using this controlled fluorination method with Fe₃O₄ nanoparticles showed that one can achieve partial or surface oxyfluoride formation at a fluorination temperature of 150 °C.²⁹ Surprisingly, even formation of a surface oxyfluoride layer improved the electrochemical performance significantly, by increasing the redox potential and improving capacity retention. In the study described here, we systematically varied the degree of fluorination from surface to bulk and correlated the changes in structure and chemical phase with electrochemical performance. To avoid the complexity of mixed-valent Fe in Fe₃O₄, we used Fe₂O₃ as the starting material. We notice interesting changes in composition as well as particle morphology of Fe₂O₃ as we varied the fluorination temperature. At 175 and 225 °C, we notice surface fluorination of Fe₂O₃ forming surface oxyfluoride species; while at 275 °C fluorination reaction, we observe transition from a bulk oxide to fluoride phase with final composition being 80% FeF₃ and 20% Fe₂O₃. Direct fluorination of the oxide yielded improved electrochemical capacity with a concomitant increase in the voltage plateau. We discuss the formation energies and plausible mechanistic pathways from oxide to fluoride without forming the intermediate oxyfluoride phase. Lithium diffusion coefficients (or apparent diffusion coefficients in the conversion regime) of the surface oxyfluoride and mixed

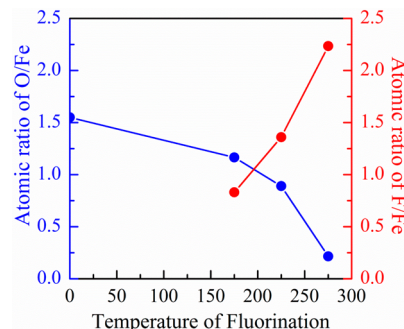


Figure 1. Change in the atomic ratio of O/Fe and F/Fe with increasing fluorination temperatures. Results were calculated from the XPS of the O 1s, F 1s, and Fe 3p peaks.

fluoride-oxide phases was studied using potentiometric intermittent titration (PITT) and electrochemical impedance spectroscopy (EIS).

RESULTS AND DISCUSSION

The initial sample weight and weight gain due to fluorination are listed in Table 1. The increased weight gain at higher temperature indicated a greater substitution of O by F. This trend was also verified by the change in the atomic ratios for F/Fe and O/Fe from the XPS study (Figure 1). The percentage of Fe₂O₃ converted to FeF₃ increased from 9.6% to 70.3% as the fluorination temperature increased from 175 to 275 °C. At lower fluorination temperatures, the surface concentration of fluorine (calculated from XPS) was much higher than the overall bulk concentration (calculated from the weight change), indicating that the surface was converted to fluoride, while the core of the particle remained oxide. After fluorinating at 275 °C the surface and bulk stoichiometry were more similar, consistent with more complete fluorination throughout the particle. More detailed XPS analysis will be discussed below.

XRD was performed to evaluate possible phase changes that occur during fluorination (Figure 2). At lower fluorination temperatures (175 and 225 °C), no phase change was observed, although the calculated percentage of reacted Fe₂O₃ was already 20.3% for the 225 °C fluorination. Possibly, amorphous or very thin layers of crystalline F-containing phase may have formed on the surface, which could not be detected by XRD. When the fluorination temperature was further increased to 275 °C, the phase change was clearly

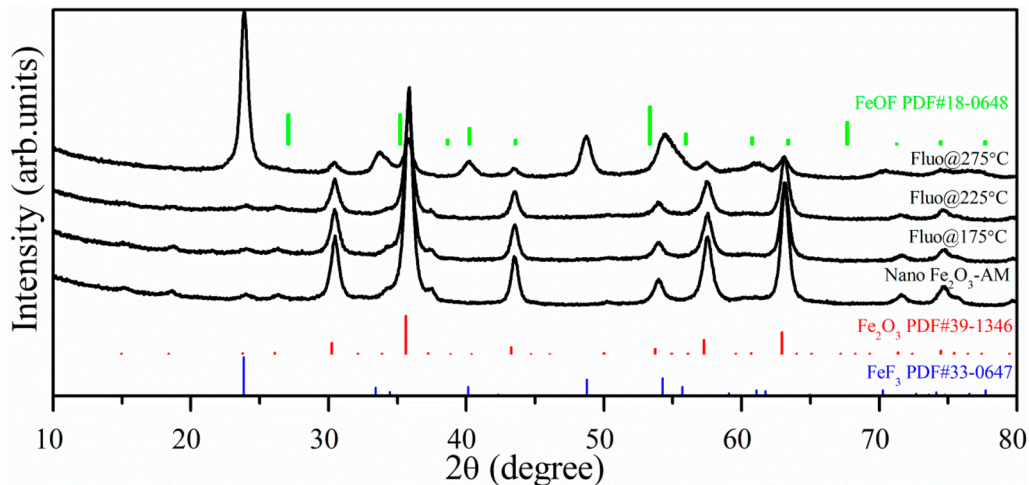


Figure 2. Comparison of XRD patterns for the Fe_2O_3 samples before and after fluorination.

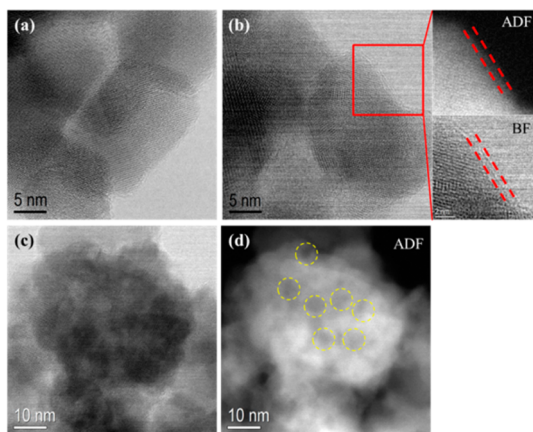


Figure 3. STEM bright field (BF) images of (a) pristine Fe_2O_3 , (b) Fe_2O_3 fluorinated at 225 °C, and (c) Fe_2O_3 fluorinated at 275 °C. (d) STEM annular dark-field (ADF) image of the sample fluorinated at 275 °C, acquired simultaneously with image c, showing the porous structure of the particles. The insets in image b are enlarged versions of the simultaneously acquired BF and ADF images showing the presence of a semicrystalline surface thin layer. The ADF contrast level of the thin layer indicates that it contains Fe compounds, which was further revealed to be F-rich by EELS spectrum imaging.

observed in the diffraction patterns; FeF_3 became the dominant phase and only minor amounts of Fe_2O_3 remained unreacted. The weight fractions of the Fe_2O_3 and FeF_3 phase obtained from Rietveld refinement were 23% and 77%, respectively (Supporting Information, Figure S1), in good agreement with the values obtained from weight change. In the fluorination temperature range from 175 °C to 275 °C, no FeOF phase was detected by XRD. Scanning transmission electron microscopy coupled with electron energy loss spectroscopy (STEM-EELS) was undertaken to investigate the possible formation of minor or amorphous phases which could not be detected by XRD.

STEM was performed on the pristine Fe_2O_3 sample, and the samples that were fluorinated at 225 °C and

275 °C. As shown in Figure 3a, the primary particle size of the starting material (nano- Fe_2O_3) was about 20 nm with well-resolved lattice fringes for whole particles. After fluorination at 225 °C, no significant change was observed except for the formation of a very thin semicrystalline or disordered layer on the surface of the particle (see enlarged area of Figure 3b). When the fluorination temperature was further increased to 275 °C, the particle morphology changed considerably. The particles were no longer dense; instead, they formed ~40–60 nm porous aggregates with many lower-density regions visible (the lattice density is 4.90 g/cm³ for Fe_2O_3 , PDF No. 39-1346 and 3.60 g/cm³ for FeF_3 , PDF No. 33-0647) in the STEM-ADF image (highlighted by the yellow circles in Figure 3d). This morphology change was likely caused in part by the volume expansion during the phase transformation from Fe_2O_3 to FeF_3 (the molar volume of Fe_2O_3 and FeF_3 are 29.0 and 31.3 cm³/mol, respectively, and one Fe_2O_3 converts to two FeF_3 during fluorination).

To measure the fluorine distribution, chemical mapping via STEM-EELS spectrum imaging was performed on two fluorinated samples. Elemental mapping (Figure 4a) showed that after fluorination at 225 °C, a fluorine-rich layer formed on the surface of the particles. Figure 4b shows that the EELS signal from the F K-edge was much stronger from the surface of the particle than from the center. Also, a shift of the Fe L-edge could be seen, due to the substitution of O with F. For the sample fluorinated at 275 °C, elemental mapping (Figure 5a) showed that F-rich domains (FeF_3 -like) and O-rich domains (Fe_2O_3 -like) were interconnected within the same particle. A chemical shift of the Fe L-edge (Figure 5b) was also observed between the F-rich and O-rich domains, due to the different local bonding.

It is noteworthy to mention that the EELS elemental maps presented here are the projected density of a specific element over the whole thickness of the particle. For positions close to the edges of the particle,

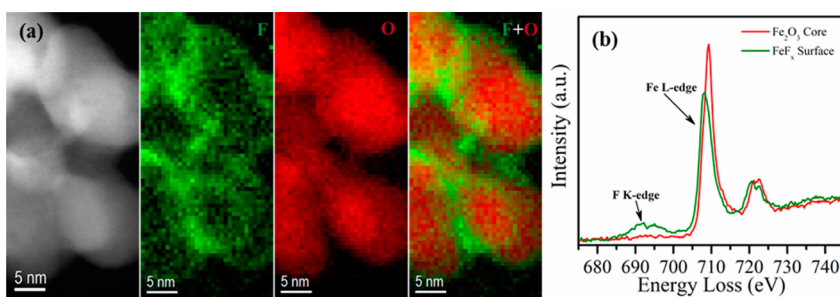


Figure 4. (a) Elemental mapping of the sample fluorinated at 225 °C and (b) corresponding EELS spectra for the surface and center part of the particle.

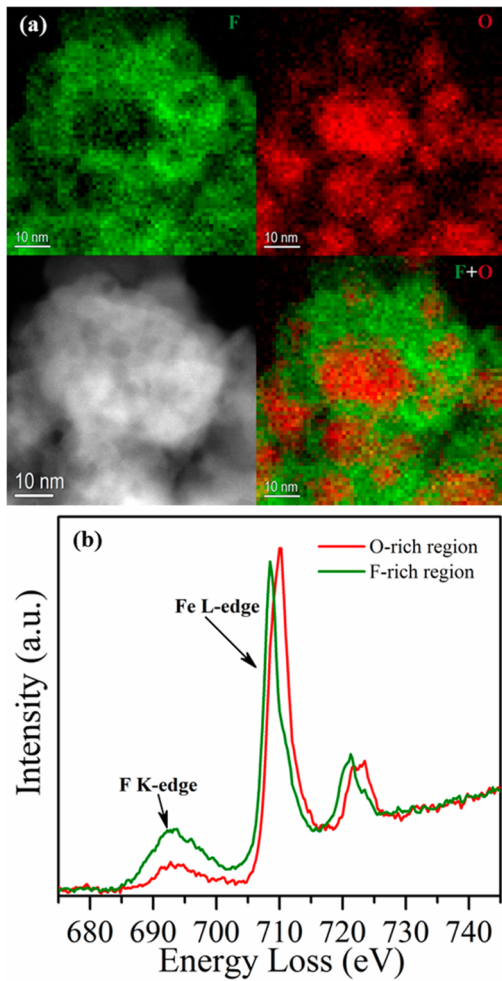


Figure 5. (a) Elemental mapping of the sample fluorinated at 275 °C and (b) corresponding EELS for the F-rich and O-rich domains.

most of the information is from the surface; and as it goes toward the center of the particle (in projection view), the EELS signals would cover mostly bulk plus the top and bottom surfaces.

XPS and STEM-EELS analysis indicated that the fluorination preferentially started from the surface and moved toward the core of the particle, but it was not uniform across the particle. To further characterize the change in the oxidation state of the surface Fe with fluorination, a detailed analysis of Fe 3p and Fe 3s core

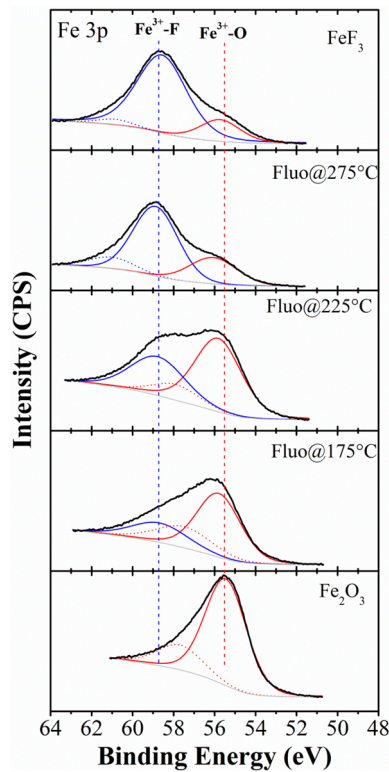


Figure 6. Fe 3p photoelectron spectra of the Fe₂O₃ samples before and after fluorination. The spectral deconvolution is also shown. The solid blue and red lines indicate the positions of the Fe³⁺-F and Fe³⁺-O bonds, respectively, using FeF₃ and Fe₂O₃ as references.

level photoelectron spectra was performed (Figures 6 and 7). The spectral deconvolution was complicated due to the multiplet structure originating from the Fe 3p–3d exchange interaction and the intrinsic spin–orbit coupling (3p_{3/2} and 3p_{1/2}).^{30,31} Since the spin–orbit coupling energy is much smaller, we did not consider this in the spectral fitting and account only for the multiplet effect, which is represented by the dashed lines in Figure 6. The Fe 3p spectra of pristine FeF₃ and Fe₂O₃ are shown for reference. The spectrum of Fe₂O₃ could be represented by two peaks, the primary Fe³⁺-O feature around 55.6 eV (red solid line) and a contribution from the multiplet splitting around 57.5 eV (red dashed line) consistent with a previous report.³² FeF₃ had the main Fe³⁺-F peak around

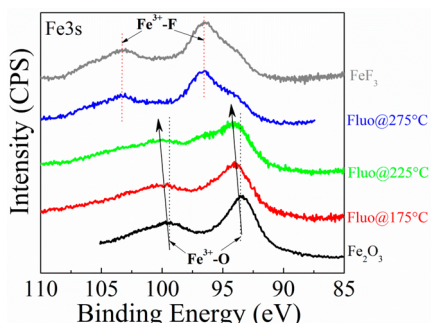


Figure 7. Fe 3s photoelectron spectra of the Fe_2O_3 samples before and after fluorination. The black and red dashed lines indicate the positions of the Fe_2O_3 and FeF_3 reference compounds. Arrows indicate the shift toward higher binding energy with increasing fluorination.

58.8 eV (blue solid line) together with its multiplet peak around 61.0 eV. Further, pristine FeF_3 also showed a surface oxidized species $\text{Fe}^{3+}-\text{O}$, which was represented by an additional peak at lower binding energy. Upon fluorination, two major peak shifts were seen: the $\text{Fe}^{3+}-\text{O}$ feature moved toward higher BE (red solid line) and another high BE component appeared that was more typical of the $\text{Fe}^{3+}-\text{F}$ environment. The BE shift followed the trend expected for more electronegative F atoms substituting for O around Fe. As expected, the $\text{Fe}^{3+}-\text{F}$ component became more and more dominant with increasing fluorination temperature. At the highest fluorination temperature of 275 °C, the spectrum looked almost identical to the FeF_3 reference compound. The XPS data indicated that the surface of the sample had mostly converted to the FeF_3 phase, consistent with observations from XRD and EELS.

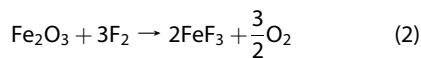
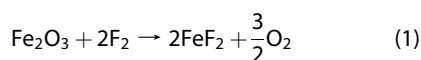
Fe 3s photoelectron spectra of the samples before and after fluorination are compared in Figure 7. Fe 3s XPS spectra typically exhibit a doublet structure, which originates from the exchange coupling between the 3s vacancy and the 3d electrons.³³ With increasing fluorination temperature, the Fe 3s peaks gradually shifted toward higher binding energy (indicated with arrows). Again, this shift was consistent with the substitution of more electronegative F for O. At a fluorination temperature of 275 °C, the Fe 3s spectrum became very similar to that of the FeF_3 reference. Although the dominant phase at 275 °C was FeF_3 , a small shoulder remained on the lower BE side indicating some Fe–O bonds were present at the surface.

On the basis of the above studies, the fluorination proceeded as follows. Initially, at lower fluorination temperatures, a thin F-rich layer formed on the surface of the particles. This amorphous or semicrystalline shell had a nominal stoichiometry of $\text{Fe}_{2-\chi}\text{O}_{3-\chi}\text{F}_{2\chi}$. Evidence for formation of an oxyfluoride surface layer was reported by us earlier for Fe_3O_4 nanoparticles.²⁹ With increased fluorination temperature (above 250 °C), F penetrated further into the Fe_2O_3 particles, and at the same time, the FeF_3 phase began to crystallize. Finally,

TABLE 2. Gibbs Free Energy of Formation (ΔG_f) for Fe_2O_3 , FeF_2 , and FeF_3

	ΔG_f (kJ/mol)		
	Fe_2O_3	FeF_2	FeF_3
175 °C	-701	-642	-938
225 °C	-688	-635	-927
275 °C	-675	-628	-916

at the highest fluorination temperature studied here (275 °C), interconnected F-rich (FeF_3) and O-rich (Fe_2O_3) domains coexisted within the particles. Importantly, no evidence of oxyfluoride phase (FeOF) was observed. It is unknown whether the FeOF phase can form at higher temperature on fluorination. Possible reaction pathways were analyzed based on their relative formation energies. The three possible fluorination reactions were as follows:



The formation energies of Fe_2O_3 and the different fluoride products were compared to determine which reaction was favored during the fluorination process (Table 2). No formation energy data have been reported for iron oxyfluorides. From a thermodynamic perspective, fluorinating Fe_2O_3 would favor the FeF_3 phase over FeF_2 .

First principle-based thermodynamic calculations from Vincent and co-workers for conversion of FeF_3 to FeOF predicted a slightly lower formation energy of $\text{Fe}_2\text{O}_3+\text{FeF}_3$ compared to that of FeOF .²⁷ This was hypothesized to be due to a higher entropic stabilization energy for FeOF . Experimental results from Amatucci's group²⁶ showed that annealing FeF_2 in air did not form FeOF even at 300 °C suggesting that FeF_2 was the more stable phase. Previous studies reported that FeOF could be synthesized by heating a mixture of Fe_2O_3 and FeF_3 at 950 °C.²⁸ A recent report by Zhang *et al.* showed that Fe_2O_3 was fully converted to FeF_3 after undergoing fluorination under an inert gas containing fluorine at 475 °C for 5 h.³⁴ Therefore, the direct conversion of the oxide to the fluoride phase during fluorination at moderate temperatures (275 °C) would be consistent with prior literature reports. Intermediate fluorination temperatures (<250 °C) could have produced $\text{Fe}_{2-\chi}\text{O}_{3-\chi}\text{F}_{2\chi}$ ($\chi < 1$) phases as demonstrated by us earlier for Fe_3O_4 . If an oxyfluoride formed, it was localized on the surface of the particles or at the interface between the oxide and fluoride domains.

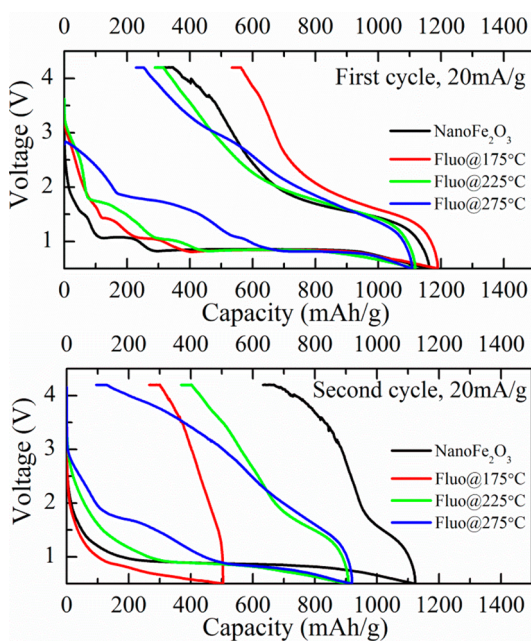
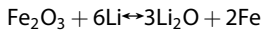


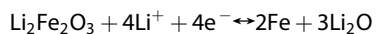
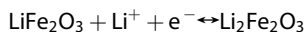
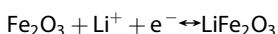
Figure 8. Voltage profiles of the first two cycles for the pristine Fe_2O_3 powder and Fe_2O_3 fluorinated at 175, 225, and 275 °C. Electrodes were cycled in the voltage range of 4.2–0.5 V with a current density of 20 mA/g.

Finally, the effect of fluorination on the electrochemical properties was evaluated. The first two charge–discharge cycles of the pristine Fe_2O_3 and the fluorinated samples were compared (Figure 8). It is to be noted that the starting pristine Fe_2O_3 nanopowder was purchased from a commercial supplier and does not have good capacity retention after the first few cycles. So in this study we only focus on the relative improvements in the electrochemical performance upon fluorination during the initial few cycles and their corresponding changes in composition, microstructure, and lithium diffusivity. The observed first cycle discharge capacities are higher than the respective theoretical capacities which could be due to side reactions from factors such as electrolyte decomposition due to lower discharge cutoff voltage (0.5 V).

The electrochemical reaction between Fe_2O_3 and Li can be expressed as



A total of six electrons are involved in the reaction which yields a theoretical capacity of 1005 mAh/g. The overall half-cell reaction of the cathode can be divided into three parts:^{35,36}

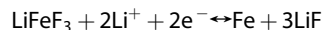
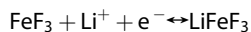


The first two reactions generally occur above 1.0 V and involve the intercalation of lithium with the reduction

of iron from Fe^{3+} to Fe^{2+} . The third step is a conversion reaction where the iron is fully reduced at a reaction plateau of about 0.8 V.

For the pristine Fe_2O_3 , three clear reaction steps were evident. Voltage plateaus occurred at 1.5 and 1.1 V for intercalation reactions and at 0.8 V for conversion (upper panel of Figure 8). After fluorination at 175 °C, minimal change was evident except for a slightly higher discharge capacity above 0.8 V due to the small amount of surface fluorination. Increasing the fluorination temperature to 225 °C resulted in two sloping discharge steps above 2.0 V and between 2.0 and 1.1 V, which closely resembled the electrochemical behavior of iron oxyfluoride as reported earlier. The coexistence of Fe–F and Fe–O bonds yielded an intercalation potential between 2.0 and 3.0 V, with the conversion plateau around 2.0 V, making this phase highly desirable for conversion-based electrochemical energy storage.

When the sample was fluorinated at 275 °C to achieve bulk fluorination, the lithiation character of FeF_3 was clearly evident in the intercalation region around 2.8 V and conversion reaction around 1.8 V. The electrochemical reaction between FeF_3 and Li is similar to its oxide counterpart, and also requires both intercalation and conversion reactions.¹⁵



To clearly observe the change in the redox potential after fluorination, the dQ/dV curves of the first cycling profile were compared for pristine Fe_2O_3 and samples fluorinated at 175, 225, and 275 °C (Figure 9a). For the pristine Fe_2O_3 , two reduction peaks at around 1.1 and 0.8 V were present, together with another very weak peak at 1.5 V, which coincided well with the three steps of the lithiation reactions. A broad oxidation at around 1.6 V was attributed to a combination of the deconversion and deintercalation reactions in the subsequent delithiation process. Lower temperature fluorination (175 °C) brought little change to the redox potentials, except for a minor increase of the intercalation potential. When the fluorination temperature was increased to 225 °C, more character from the F-containing phase was observed: the reduction peak at 1.5 V shifted to 1.7 V and a broad reduction peak around 2.75 V emerged, corresponding to the conversion and intercalation reaction of the fluoride phase. In addition, a shoulder on the higher voltage side was observed for the oxidation peak. The electrochemical character of iron fluoride was apparent in the sample fluorinated at 275 °C: the reduction peaks shifted further to 1.8 and 2.8 V and another oxidation peak appeared at 3.0 V. Overall, with fluorination, the noticeable redox features transitioned from Fe_2O_3 to FeF_3 . At intermediate temperatures more mixed character was present.

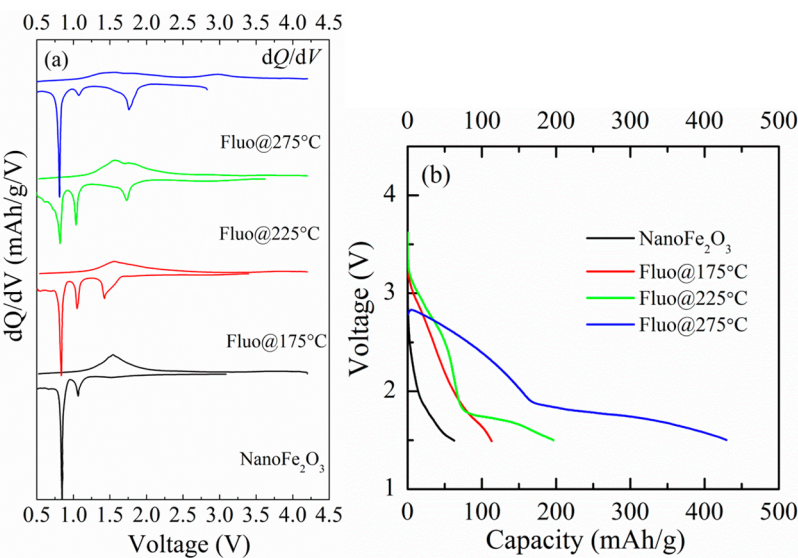


Figure 9. (a) dQ/dV of the first cycling profile for the pristine Fe_2O_3 powder and Fe_2O_3 fluorinated at 175, 225, and 275 °C; (b) 1st discharge profile with 1.5 V cutoff of Fe_2O_3 and the fluorinated samples at 175, 225, and 275 °C showing increase in capacity contribution at higher voltage.

To ascertain the practical significance of the increased voltage plateau with fluorination, we studied the discharge behavior of the fluorinated samples with 1.5 V cutoff voltage as shown in Figure 9b. The profile clearly shows increased capacity contribution at higher voltage as expected for the oxyfluoride composition. As reported earlier (ref 1) the large increase in surface area of the active material after the conversion reaction is one of the main reasons responsible for increasing the voltage hysteresis. In our case, the mixed phase formation of Fe_2O_3 and FeF_3 would have even more phase separation during discharge (not just Fe and Li_2O , but also Fe and LiF), and hence higher voltage overpotential during the charge. Interestingly, the voltage hysteresis for pristine Fe_2O_3 sample is significantly larger than the mixed phase (Figure 8) for the second cycle.

To further investigate the transport mechanism and the observed electrochemical performance of the fluorinated Fe_2O_3 samples, we carried out combined PITT and EIS studies to measure the lithium-ion diffusivities (or apparent diffusivity in the conversion regime) based on analysis reported earlier by Ko *et al.*³⁷ for iron fluorides and oxyfluorides. Detailed analysis and the model calculations to estimate the lithium-ion diffusion coefficients (D_{Li}) and the experimental results are discussed in the Supporting Information. Figure 10 shows the estimated Li-ion diffusivity of Fe_2O_3 and fluorinated analogues as a function of the discharge voltage. It was not possible to measure D_{Li} in the samples fluorinated at 275 °C by EIS since no 45° line characteristic of the Warburg impedance was observed in these samples over the measured frequency range.

Some interesting trends emerge from Figure 10. The diffusion coefficients measured by EIS are typically an order of magnitude larger than those measured by PITT. This can be partly attributed to the simplifying

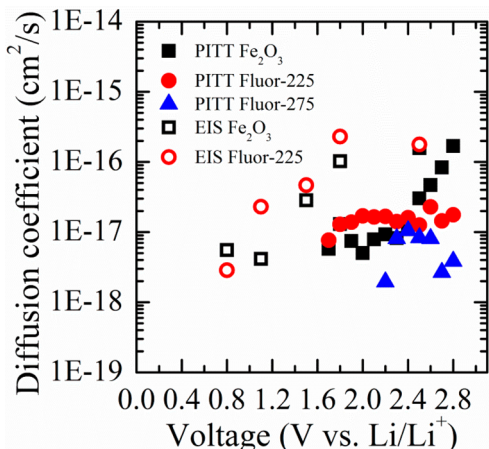


Figure 10. Diffusion coefficients measured by PITT and EIS at different potentials during discharge.

assumptions made in the analysis such as the average particle size and assuming a uniform size distribution. Further, the cells in the EIS measurements were also discharged at a faster rate than in the PITT measurements and are therefore further from equilibrium. In general, we notice about 1–2 orders of magnitude decrease in D_{Li} moving from the intercalation regime to the conversion regime consistent with prior work on iron fluorides.³⁷ The sample fluorinated at 225 °C has a similar diffusion coefficient as the unfluorinated Fe_2O_3 over most of the voltage range. This is expected since fluorination at 225 °C leaves a majority Fe_2O_3 phase. The slowest diffusion coefficients were measured for the mixed phase composition (275 °C) which has a majority FeF_3 phase (77%). FeF_3 has been reported to have D_{Li} in the range of 10^{-18} cm^2/s which is in good agreement with the values reported here.³⁷ Due to the extremely slow kinetics of such systems especially in

the conversion regime we only could estimate the apparent diffusion coefficient up to 1.6 V. Further at lower voltages the current decay steps were too noisy for any meaningful analysis.

CONCLUSIONS

We report a direct fluorination method under fluorine gas atmosphere using a fluidized bed reactor for converting nanoparticle iron oxide ($n\text{-Fe}_2\text{O}_3$) to electrochemically stable and higher energy density iron oxyfluoride/fluoride phase. The degree of fluorination was controlled by varying the reaction bed temperature while maintaining a constant flow rate of the $\text{F}_2\text{-N}_2$ mixture. For Fe_2O_3 nanoparticles, fluorination at 175 and 225 °C led to formation of a thin amorphous layer of oxyfluoride on the surface as verified by STEM-EELS and XPS analysis. Formation of a surface oxyfluoride rich layer was also observed earlier by us for $n\text{-Fe}_3\text{O}_4$ conversion oxides. Interestingly, fluorination at 275 °C yielded mixed phases of Fe_2O_3 and FeF_3 instead of bulk oxyfluoride with X-ray Rietveld refinement showing 77% FeF_3 and the remainder being the Fe_2O_3 phase. Further, particles fluorinated at 275 °C have unique morphology and phase with STEM-EELS results showing porous interconnected nanodomains of FeF_3 and Fe_2O_3 coexisting within the same particle while overall the particles become less dense after fluorination. With increased fluorination temperature we notice a gradual increase of the voltage profiles to higher voltage corresponding to the increase in ionic

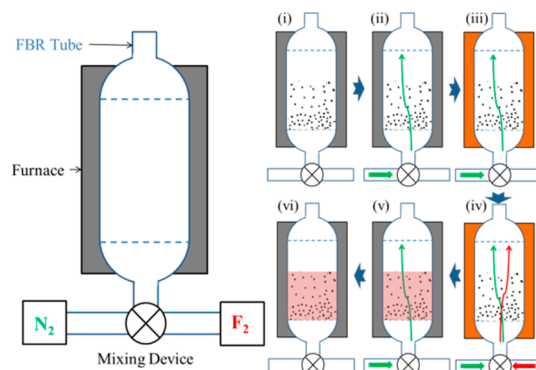


Figure 11. Diagram of the fluidized bed reactor (FBR) used for fluorination (left) and the fluorination procedure (right): (i) load sample; (ii) purge FBR tube; (iii) heat furnace; (iv) introduce F_2 and start reaction; (v) stop reaction and purge the tube; (vi) collect the fluorinated sample.

character of metal fluoride bonds. Interestingly, the discharge profile for the 275 °C sample shows an interesting mix of FeF_3 and Fe_2O_3 electrochemical behavior in agreement with the X-ray and microstructural results. We investigated the trends in lithium diffusivity (or apparent diffusivity) in both the intercalation and conversion regimes for the pristine and fluorinated Fe_2O_3 from PITT as well as EIS measurements. Our approach demonstrates the ability to tune the electrochemical and chemical functionality of high capacity conversion-based materials by altering their molecular architecture and the nature of the chemical bonds.

METHODS

Materials Synthesis. All fluorinations were conducted in a fluidized bed reactor (FBR) (Figure 11). The reactor was connected to a mixing device consisting of a Hastings flow transducer for fluorine and a rotameter gauge flowmeter for nitrogen gas. The fluorine source was 20% F_2 in N_2 . All reported flow rates for F_2 were corrected for this dilution factor. Before fluorination, the Fe_2O_3 nanopowders (Inframat Advanced Materials LLC, CT, USA) were dried at 150 °C under vacuum (<10 mTorr) overnight. The dehydrated sample powder was weighed and placed in an FBR tube sealed by Teflon tape. The FBR tube was purged for 30 min with 46 sccm N_2 prior to ramping the temperature to the set temperature (175, 225, or 275 °C). Once the desired temperature was achieved, fluorine gas was introduced into the reactor along with the N_2 flow. After the allotted reaction time the FBR was allowed to cool under continuous N_2 purge. The Fe_2O_3 samples were weighed in the FBR before and after fluorination to eliminate transfer losses in the gravimetric determinations. Then the samples were transferred under nitrogen. The FBR method used for the conversion of iron oxide to oxyfluorides/fluorides used low pressure fluorine gas mixed with an inert carrier gas (N_2). This is a relatively simple and safe process that is used routinely for fluorination studies.³⁸ The experimental conditions for fluorination are summarized in Table 1. Many different factors can potentially control fluorination, such as the morphology of the starting material, temperature, reaction time, and partial pressure of F_2 . Here, we varied the fluorination temperature while keeping other conditions constant.

Material Characterization. The structure of the samples was characterized by X-ray powder diffraction (XRD) using a Scintag PDS 2000 diffractometer equipped with Cu $\text{K}\alpha$ source and Ni

filter ($\lambda = 1.54178 \text{ \AA}$). Data were collected over the range of 5–90° 2θ with a step size of 0.02° and dwell time of 1 s; a longer dwell time (15 s) was used for the refinement of the XRD data. The Rietveld refinement of the XRD patterns was done using the GSAS/EXPGUI package.³⁹ Surface chemistry and composition analysis was measured by X-ray photoelectron spectroscopy (XPS) using a PHI 3056 spectrometer with an Al source in a 2×10^{-8} Torr vacuum chamber. High resolution scans were taken with 23.5 eV pass energy, 0.05 eV energy step, and 80–100 repeats to improve the signal-to-noise ratio. Survey scans were measured at 93.9 eV pass energy, 0.25 eV energy step, and 10 repeats. The C 1s XPS core level spectrum at a BE value of 284.8 eV arising from the adventitious carbon was used as a reference to correct for sample charging. The surface atomic concentrations were calculated by integrating the peak areas and using the standard atomic sensitivity factors supplied by the equipment manufacturer. The spectra were deconvoluted through Gaussian–Lorentzian functions after a Shirley-type background subtraction. The local crystal structure and composition were further analyzed using an aberration corrected Nion UltraSTEM-200 scanning transmission electron microscope,⁴⁰ operated at 200 kV. The TEM specimens were prepared by dispersing the powders onto lacey carbon grids inside a glovebox. The convergence semiangle for the focused electron beam was set to 30 mrad. Bright field (BF) and annular dark field (ADF) images were collected simultaneously from the sample. The STEM-BF images contain phase contrast images, showing the arrangement of the lattice planes. The STEM-ADF image contrast is directly related to the atomic number at the imaging area, averaged over the thickness direction. Chemical maps were obtained via electron energy loss spectrum imaging using the Fe L-edge, O K-edge, and F K-edge.

Electrochemical Testing. The electrochemical properties of these samples were evaluated in two-electrode coin-type cells (size 2032, Hohsen Corp. Japan) on a MacCor multichannel battery tester (model 4000, MacCor Inc., Tulsa, OK, USA) using pure lithium foil (purity 99.9%, Alfa Aesar) as the counter electrode. A tape casting slurry for each sample was prepared by mixing the sample powder, multilayer graphene (MLG, Graphene Supermarket), and PVDF (poly(vinylidene fluoride)) powder in a weight ratio of 50:40:10 in NMP (*N*-methylpyrrolidone) with a Turbula Shaker-Mixer (Glen Mills Inc., NJ, USA). After mixing for about 30 min, the homogeneous slurry was tape-casted on Al foil and then dried under vacuum at 90 °C overnight. The typical loading of the cathode was around 2 mg/cm² with an electrode area of 1.0 cm². The electrolyte was 1.2 M LiPF₆ (lithium hexafluorophosphate) dissolved in a mixture of EC (ethylene carbonate) and DMC (dimethyl carbonate) (battery grade, Novolyte Technologies, USA) in a volume ratio of 3:7 with HF and H₂O impurities less than 50 and 5 ppm, respectively. Celgard 2325 separators (Celgard Inc., USA) were used. The coin cells were assembled in a high purity argon filled glovebox. The charge–discharge cycling (at 25 °C) was performed between 0.5 and 4.2 V with a current density of 20 mA/g. PITT and EIS analysis were performed using a Bio-Logic VSP potentiostat. For PITT the voltage was stepped down in 10 mV increments. The potential was held constant at each step until the current relaxed to <200 μA/g. The diffusion coefficient (or apparent diffusion coefficients in the conversion regime) were calculated from the linear slope in plots of ln (I) vs $t^{1/2}$.^{37,41} All particles were treated as 20 nm spheres on the basis of electron microscopy results. For EIS the cells were discharged at 20 mA/g and EIS data were collected at several different voltages during the discharge. The potential was held constant at each voltage of interest for 2 h to allow the current to relax prior to EIS measurement. EIS data were collected over the frequency range from 1 MHz to 10 mHz using a 10 mV sinusoidal perturbation. Diffusion coefficients were calculated from the low frequency Warburg impedance by taking the slope of Re(Z) vs $\omega^{-1/2}$.^{37,41} The active surface area was estimated from the electrode loading by assuming 20 nm spherical particles in all cases.

Conflict of Interest: The authors declare no competing financial interest.

Acknowledgment. This research was supported by the Laboratory Directed Research and Development Program of Oak Ridge National Laboratory, managed by UT-Battelle, LLC, for the U.S. Department of Energy. The microscopy work was supported by a Wigner Fellowship through the Laboratory Directed Research and Development Program of Oak Ridge National Laboratory, managed by UT-Battelle, LLC, for DOE (WZ). The microscopy was performed on the Nion UltraSTEM200 at ORNL, supported by DOE BES Materials Sciences and Engineering Division. J.A. and S.D. were supported by the U.S. Department of Energy's Office of Basic Energy Science, Division of Materials Sciences and Engineering. We thank Gabriel Veith for discussion and assistance with XPS measurements and Juchuan Li for assistance with PITT measurements.

Supporting Information Available: Rietveld refinement for the XRD data of the sample fluorinated at 275 °C, comparison of EELS for the samples fluorinated at 225 and 275 °C, filtered F phase spatial distribution on the ADF image of the sample fluorinated at 275 °C, and details of PITT and EIS analysis. This material is available free of charge via the Internet at <http://pubs.acs.org>.

REFERENCES AND NOTES

- Cabana, J.; Monconduit, L.; Larcher, D.; Palacin, M. R. Beyond Intercalation-Based Li-Ion Batteries: The State of the Art and Challenges of Electrode Materials Reacting through Conversion Reactions. *Adv. Mater.* **2010**, *22*, E170–E192.
- Zhang, J.; Wang, R.; Yang, X.; Lu, W.; Wu, X.; Wang, X.; Li, H.; Chen, L. Direct Observation of Inhomogeneous Solid Electrolyte Interphase on MnO Anode with Atomic Force Microscopy and Spectroscopy. *Nano Lett.* **2012**, *12*, 2153–2157.
- Ban, C.; Wu, Z.; Gillaspie, D. T.; Chen, L.; Yan, Y.; Blackburn, J. L.; Dillon, A. C. Nanostructured Fe₃O₄/SWNT Electrode: Binder-Free and High-Rate Li-Ion Anode. *Adv. Mater.* **2010**, *22*, E145–E149.
- Thackeray, M. M.; Coetzer, J. A Preliminary Investigation of the Electrochemical Performance of Alpha-Fe₂O₃ and Fe₃O₄ Cathodes in High-Temperature Cells. *Mater. Res. Bull.* **1981**, *16*, 591–597.
- Zhang, L.; Wu, H. B.; Madhavi, S.; Hng, H. H.; Lou, X. W. Formation of Fe₂O₃ Microboxes with Hierarchical Shell Structures from Metal–Organic Frameworks and their Lithium Storage Properties. *J. Am. Chem. Soc.* **2012**, *134*, 17388–17391.
- Chen, J.; Xu, L. N.; Li, W. Y.; Gou, X. L. Alpha-Fe₂O₃ Nanotubes in Gas Sensor and Lithium-Ion Battery Applications. *Adv. Mater.* **2005**, *17*, 582–586.
- Koo, B.; Xiong, H.; Slater, M. D.; Prakapenka, V. B.; Balasubramanian, M.; Podsiadlo, P.; Johnson, C. S.; Rajh, T.; Shevchenko, E. V. Hollow Iron Oxide Nanoparticles for Application in Lithium Ion Batteries. *Nano Lett.* **2012**, *12*, 2429–2435.
- Li, L.; Yu, Y.; Meng, F.; Tan, Y.; Hamers, R. J.; Jin, S. Facile Solution Synthesis of α-FeF₃·3H₂O Nanowires and Their Conversion to α-Fe₂O₃ Nanowires for Photoelectrochemical Application. *Nano Lett.* **2012**, *12*, 724–731.
- Li, Y.; Tan, B.; Wu, Y. Mesoporous Co₃O₄ Nanowire Arrays for Lithium Ion Batteries with High Capacity and Rate Capability. *Nano Lett.* **2007**, *8*, 265–270.
- Dalverny, A. L.; Filhol, J. S.; Doublet, M. L. Interface Electrochemistry in Conversion Materials for Li-Ion Batteries. *J. Mater. Chem.* **2011**, *21*, 10134–10142.
- Lee, D. H.; Carroll, K. J.; Calvin, S.; Jin, S.; Meng, Y. S. Conversion Mechanism of Nickel Fluoride and NiO-Doped Nickel Fluoride in Li Ion Batteries. *Electrochim. Acta* **2012**, *59*, 213–221.
- Yamakawa, N.; Jiang, M.; Grey, C. P. Investigation of the Conversion Reaction Mechanisms for Binary Copper(II) Compounds by Solid-State NMR Spectroscopy and X-ray Diffraction. *Chem. Mater.* **2009**, *21*, 3162–3176.
- Oumella, Y.; Rougier, A.; Nazri, G. A.; Tarascon, J. M.; Aymard, L. Metal Hydrides for Lithium-Ion Batteries. *Nat. Mater.* **2008**, *7*, 916–921.
- Li, L.; Meng, F.; Jin, S. High-Capacity Lithium-Ion Battery Conversion Cathodes Based on Iron Fluoride Nanowires and Insights into the Conversion Mechanism. *Nano Lett.* **2012**, *12*, 6030–6037.
- Badway, F.; Cosandey, F.; Pereira, N.; Amatucci, G. G. Carbon Metal Fluoride Nanocomposites: High-Capacity Reversible Metal Fluoride Conversion Materials as Rechargeable Positive Electrodes for Li Batteries. *J. Electrochem. Soc.* **2003**, *150*, A1318–A1327.
- Zhang, N.; Yi, R.; Wang, Z.; Shi, R.; Wang, H.; Qiu, G.; Liu, X. Hydrothermal Synthesis and Electrochemical Properties of Alpha-Manganese Sulfide Submicrocrystals as an Attractive Electrode Material for Lithium-Ion Batteries. *Mater. Chem. Phys.* **2008**, *111*, 13–16.
- Li, T.; Chen, Z. X.; Cao, Y. L.; Ai, X. P.; Yang, H. X. Transition-Metal Chlorides as Conversion Cathode Materials for Li-Ion Batteries. *Electrochim. Acta* **2012**, *68*, 202–205.
- Wang, Z.; Luan, D.; Madhavi, S.; Hu, Y.; Lou, X. W. Assembling Carbon-Coated Alpha-Fe₂O₃ Hollow Nanohorns on the CNT Backbone for Superior Lithium Storage Capability. *Energy Environ. Sci.* **2012**, *5*, 5252–5256.
- Reddy, M. V.; Yu, T.; Sow, C. H.; Shen, Z. X.; Lim, C. T.; Subba Rao, G. V.; Chowdari, B. V. R. Alpha-Fe₂O₃ Nanoflakes as an Anode Material for Li-Ion Batteries. *Adv. Funct. Mater.* **2007**, *17*, 2792–2799.
- Xu, X.; Cao, R.; Jeong, S.; Cho, J. Spindle-Like Mesoporous Alpha-Fe₂O₃ Anode Material Prepared from MOF Template for High-Rate Lithium Batteries. *Nano Lett.* **2012**, *12*, 4988–91.
- Zhou, Q.; Zhao, Z. B.; Wang, Z. Y.; Dong, Y. F.; Wang, X. Z.; Gogotsi, Y.; Qiu, J. S. Low Temperature Plasma Synthesis of

- Mesoporous Fe_3O_4 Nanorods Grafted on Reduced Graphene Oxide for High Performance Lithium Storage. *Nanoscale* **2014**, *6*, 2286–2291.
22. Badway, F.; Pereira, N.; Cosandey, F.; Amatucci, G. G. Carbon–Metal Fluoride Nanocomposites—Structure and Electrochemistry of FeF_3 : *C. J. Electrochem. Soc.* **2003**, *150*, A1209–A1218.
 23. Li, H.; Balaya, P.; Maier, J. Li-Storage via Heterogeneous Reaction in Selected Binary Metal Fluorides and Oxides. *J. Electrochem. Soc.* **2004**, *151*, A1878–A1885.
 24. Plitz, I.; Badway, F.; Al-Sharab, J.; DuPasquier, A.; Cosandey, F.; Amatucci, G. G. Structure and Electrochemistry of Carbon–Metal Fluoride Nanocomposites Fabricated by Solid-State Redox Conversion Reaction. *J. Electrochem. Soc.* **2005**, *152*, A307–A315.
 25. Amatucci, G. G.; Pereira, N. Fluoride Based Electrode Materials for Advanced Energy Storage Devices. *J. Fluorine Chem.* **2007**, *128*, 243–262.
 26. Pereira, N.; Badway, F.; Wartelsky, M.; Gunn, S.; Amatucci, G. G. Iron Oxyfluorides as High Capacity Cathode Materials for Lithium Batteries. *J. Electrochem. Soc.* **2009**, *156*, A407–A416.
 27. Chevrier, V. L.; Hautier, G.; Ong, S. P.; Doe, R. E.; Ceder, G. First-Principles Study of Iron Oxyfluorides and Lithiation of FeOF . *Phys. Rev. B* **2013**, *87*, 094118.
 28. Brink, F. J.; Withers, R. L.; Thompson, J. G. An Electron Diffraction and Crystal Chemical Investigation of Oxygen/Fluorine Ordering in Rutile-Type Iron Oxyfluoride, FeOF . *J. Solid State Chem.* **2000**, *155*, 359–365.
 29. Zhou, H.; Nanda, J.; Martha, S. K.; Adcock, J.; Idrobo, J. C.; Baggetto, L.; Veith, G. M.; Dai, S.; Pannala, S.; Dudney, N. J. Formation of Iron Oxyfluoride Phase on the Surface of Nano- Fe_3O_4 Conversion Compound for Electrochemical Energy Storage. *J. Phys. Chem. Lett.* **2013**, *4*, 3798–3805.
 30. Kozakov, A. T.; Kochur, A. G.; Googlev, K. A.; Nikolsky, A. V.; Raevski, I. P.; Smotrakov, V. G.; Yeremkin, V. V. X-ray Photoelectron Study of the Valence State of Iron in Iron-Containing Single-Crystal (BiFeO_3 , $\text{PbFe}_{1/2}\text{Nb}_{1/2}\text{O}_3$), and Ceramic ($\text{BaFe}_{1/2}\text{Nb}_{1/2}\text{O}_3$) Multiferroics. *J. Electron Spectrosc.* **2011**, *184*, 16–23.
 31. Tiedtke, K.; Gerth, C.; Martins, M.; Zimmermann, P. Term-Dependent Lifetime Broadening in the 3p Photoelectron Spectra of Atomic Fe and Co. *Phys. Rev. A* **2001**, *64*, 022705.
 32. Yamashita, T.; Hayes, P. Analysis of XPS Spectra of Fe^{2+} and Fe^{3+} Ions in Oxide Materials. *Appl. Surf. Sci.* **2008**, *254*, 2441–2449.
 33. Van Vleck, J. H. The Dirac Vector Model in Complex Spectra. *Phys. Rev.* **1934**, *45*, 405–419.
 34. Zhang, W.; Ma, L.; Yue, H.; Yang, Y. Synthesis and Characterization of *in situ* Fe_2O_3 -Coated FeF_3 Cathode Materials for Rechargeable Lithium Batteries. *J. Mater. Chem.* **2012**, *22*, 24769–24775.
 35. Thackeray, M. M.; David, W. I. F.; Goodenough, J. B. Structural Characterization of the Lithiated Iron Oxides $\text{Li}_x\text{Fe}_3\text{O}_4$ and $\text{Li}_x\text{Fe}_2\text{O}_3$ ($0 < x < 2$). *Mater. Res. Bull.* **1982**, *17*, 785–793.
 36. Wu, M.-S.; Ou, Y.-H.; Lin, Y.-P. Iron Oxide Nanosheets and Nanoparticles Synthesized by a Facile Single-Step Coprecipitation Method for Lithium-Ion Batteries. *J. Electrochem. Soc.* **2011**, *158*, A231–A236.
 37. Ko, J. K.; Wiaderek, K. M.; Pereira, N.; Kinnibrugh, T. L.; Kim, J. R.; Chupas, P. J.; Chapman, K. W.; Amatucci, G. G. Transport, Phase Reactions, and Hysteresis of Iron Fluoride and Oxyfluoride Conversion Electrode Materials for Lithium Batteries. *ACS Appl. Mater. Interfaces* **2014**, *6*, 10858–10869.
 38. Fulvio, P. F.; Brown, S. S.; Adcock, J.; Mayes, R. T.; Guo, B.; Sun, X.-G.; Mahurin, S. M.; Veith, G. M.; Dai, S. Low-Temperature Fluorination of Soft-Templated Mesoporous Carbons for a High-Power Lithium/Carbon Fluoride Battery. *Chem. Mater.* **2011**, *23*, 4420–4427.
 39. Toby, B. H. EXPGUI, a Graphical User Interface for GSAS. *J. Appl. Crystallogr.* **2001**, *34*, 210–213.
 40. Dellby, N.; Bacon, N. J.; Hrcicirik, P.; Murfitt, M. F.; Skone, G. S.; Szilagyi, Z. S.; Krivanek, O. L. Dedicated STEM for 200 to 40 keV Operation. *Eur. Phys. J.-Appl. Phys.* **2011**, *54*, 33505–33515.
 41. Wen, C. J.; Ho, C.; Boukamp, B. A.; Raistrick, I. D.; Weppner, W.; Huggins, R. A. Use of Electrochemical Methods to Determine Chemical-Diffusion Coefficients in Alloys: Application to 'LiAl'. *Int. Metal Rev.* **1981**, *26*, 253–268.